doi:10.20944/preprints202106.0156.v1

Article

Strain and grain size of CeO_2 and TiO_2 nanoparticles: Comparing structural and morphological methods

Yamerson Canchanya-Huaman [1], Angie F. Mayta-Armas [1], Jemina Pomalaya-Velasco [1], Yéssica Bendezú-Roca [1], Jorge Andres Guerra [2] and Juan A. Ramos-Guivar [3,*]

[1] Laboratorio de No Metálicos, Facultad de Ingeniería Química, Universidad Nacional del Centro del Perú (UNCP), Av. Mariscal Ramón Castilla Nº 3909, El Tambo, Huancayo 12000, Perú; yamerson2016@gmail.com (Y.C.H), armasfiorella23@gmail.com (A.F.M.A), jpomalayavelasco@gmail.com (J.P.V.), ybendezu@uncp.edu.pe (Y.B.R)

[2] Departamento de Ciencias, Sección Física, Pontificia Universidad Católica del Perú, Av. Universitaria 1801, 15088, Lima, Perú; guerra.jorgea@pucp.edu.pe (J.A.G.)

[3] Grupo de Investigación de Nanotecnología Aplicada para Biorremediación Ambiental, Energía, Biomedicina y Agricultura (NANOTECH), Facultad de Ciencias Físicas, Universidad Nacional Mayor de San Marcos, Av. Venezuela Cdra 34 S/N, Ciudad Universitaria, Lima 15081, Perú

* juan.ramos5@unmsm.edu.pe; Tel.: +51-1-914728212

Abstract: Various crystallite size estimation methods were used to analyze X-ray diffractograms of spherical cerium dioxide and donut-like titanium dioxide anatase nanoparticles aiming to evaluate their reliability and limitations. The microstructural parameters were estimated from Scherrer, Monshi, Williamson-Hall, and their variants: i) uniform deformation model, ii) uniform strain deformation model, and iii) uniform deformation energy density model, and also size-strain plot, and Halder-Wagner method. For that, and improved systematic Matlab code was developed to estimate the crystallite sizes and strain, and the linear regression analysis was used to compare all the models based on the coefficient of determination, where the Halder Wagner method gave the highest value (close to 1). Therefore, being the best candidate to fit the X-ray Diffraction data of metal-oxide nanoparticles. Advanced Rietveld was introduced for comparison purposes. Refined microstructural parameters were obtained from a nanostructured 40.5 nm Lanthanum hexaboride nanoparticles and correlated with the above estimation methods and transmission electron microscopy images. In addition, electron density modelling was also studied for final refined nanostructures, and μ-Raman spectra were recorded for each material estimating the mean crystallite size and comparing by means of a phonon confinement model.

Keywords: X-ray diffraction; CeO_2; TiO_2; crystallite size; strain; TEM; μ-Raman

1. Introduction

Nanotechnology is the branch of Science in which materials are obtained and studied on a nanometric scale, named as nanoparticles (NPs), where novel and outstanding physical and chemical effects are found between 1 and 100 nm [1]. NPs can be obtained through various physical, chemical or biological synthesis methods. The NPs manufacturing process is essential since it can affect the photocatalytic, adsorptive, thermal, and optical properties of metal oxides such as cerium oxide (CeO_2) and titanium oxide (TiO_2), which depend on the particle size, shape, and crystal morphology [2]. Hence, the tuning of structural and morphological properties is highly relevant due to their possible usefulness in different applications. For example, CeO_2 NPs are widely used due to their wide range of application in electrochemistry, such as electrode materials in supercapacitors, and medicine, due to their antibacterial properties [3]. On the other hand, TiO_2 NPs are highly used in photocatalysis, solar cells, biomedicine, chemical sensors, and lithium storage [2],and have been also explored for heavy metal water cleaning purposes [4].

doi:10.20944/preprints202106.0156.v1

Currently, physical techniques such as scanning electron microscopy (SEM), transmission electron microscopy (TEM), and atomic force microscopy (AFM) are used to estimate and confirm the NPs scale [5], as well as indirect methods such as powder X-ray diffraction (pXRD). In particular, pXRD analysis is widely used for determining crystallite size and lattice deformation. The information of the two latter physical parameters correlates the diffraction peak broadening with lattice strain which sources come from imperfections (stacking faults or coherency stresses) of the studied material. There exist several methods to estimate the peak broadening from XRD data [6]. However, the accuracy of these methods is questionable due to inconsistencies between them.

The above-mentioned pXRD methods used nowadays are modifications of the 1918 Scherrer method, which relates the peak broadening (β) of each diffracted Bragg peak to a characteristic mean size (D) [7]. Since that first work, new parameters have been added to better represent the physical effects that can be produced in the intensity distribution of diffracted X-rays. In 1953, the Williamson Hall (W-H) method introduced the general distribution of deformations ε [8], which takes into account the two-parameter effects of size and lattice strain. Generalized models, such as the uniform deformation model (UDM) considers the uniform stress in all crystallographic directions, considering the crystal of isotropic nature[9]. Whilst the mechanical Hooke's law considers the strain in the uniform deformation stress model (USDM) and uniform deformation energy density model (UDEDM), the latter methods take into account the anisotropic nature of the Young's modulus of the crystal [10]. Instead, the Halger Wagner (H-W) method implies the assumption that the spreading of the peak is a symmetric Voigt function, which means that the size of the crystallite is defined by the Lorentzian and Gaussian functions [11]. Similarly, by the size-strain plot (SSP) method, assumes that the crystallite size profile is described by a Lorentz function and the deformation profile by a Gaussian function [12].

On the other hand, Rietveld method (RM) is a tool for analyzing crystalline structures [13], which consists of theoretical refinement of the structural or cell parameters, atomic displacement, anisotropy, cell stresses, shape and anisotropy effects, among others, until a condition of convergence is reached between the values of experimental diffractogram curves and the theoretical model [14]. This refinement is suitable when calculating the microstructural parameters for a multiphasic sample (percentual concentration). For example [15], where diffraction peaks overlap and systematical errors can arise from correct determination of full width at half maximum (FWHM) values, as it can be the case in the previous discussed methods. The theoretical model includes structural aspects such as: crystalline structure, spatial group, atom Wyckoff positions, etc. In addition, microstructural information are involved including crystal size and micro-deformations, The RM also includes instrumental factors such as the optical effect of XRD equipment on the width of diffraction peaks [16]. It is worth mentioning that the RM makes use of known atomic structures to generate an initial theoretical model of the structure of the phases present in the sample, so these must be previously identified. From this initial model, the method allows to refine the structural parameters, based on the analysis of least squares [17], until the model matches the experimental profile [16].

In the present work, a comparative study of the microstructural parameters of metal-oxide CeO_2 and TiO_2 NPs has been investigated by employing different modified models including W-H, UDM, UDSM, UDEDM, SSP, and H-W. All the methods were compared to the obtained results from RM and TEM images. Additionally, crystallite size was also estimated from μ-Raman measurements by means of a phonon confinement model.

2. Materials and Methods

2.1. *X-ray and TEM experimental details*

TiO_2, CeO_2, and Lanthanum hexaboride (LaB_6) were obtained from Sigma Aldrich, and no further purification was performed to the powder samples. The pXRD data were collected using a Rigaku diffractometer, operating with CuKα radiation (1.5406 Å), at 50 kV and 100 mA. The diffractograms were collected in step scanning configuration

doi:10.20944/preprints202106.0156.v1

between 2θ =20°-100° for CeO_2 and TiO_2 , with 0.02° and 5s per step. The crystallographic phases were identified using Match version 3 software obtaining crystallographic cards [96-434-3162] and [96-500-022] with the crystallographic information file (CIF) #9009008 and #5000223 for the CeO_2 and TiO_2 anatase phases, respectively. The Origin pro 9.0 software was used to estimate the FWHM using a pseudo-Voigt fitting model. By making use of the instrumental width correction ($\beta inst$ = 0.01°); the microstructual parameters were systematically ontained by using a code in Matlab version R2017b which is given in the Supplementary material. The values for microstructural parameters estimated from the code (including corrected instrumental resolution) are close in value to the obtained by the linear fit for each crystallite estimation model. Therefore, we only reported these values in Table 1.

For the RM of the diffractograms, the software Fullprof was employed, the CeO_2 and TiO_2 crystallographic information files (CIF) obtained from Match v3 software were used as initial parameters, which crystallographic data for CeO_2 are: cubic crystalline structure, space group Fm-3m, and cell parameters a=5.4110 Å. And, for TiO_2 anatase they were: tetragonal crystalline structure, space group I 41/amd, cell parameters a=3.78435 Å, c=9.50374 Å for both cases the Caglioti's initial parameters were U=0.004133, V=-0.007618, and W= 0.006255 and refined using the pseudo-Voigt function. Finally, the average crystallite size was determined in the Fullprof program. To do that, we first characterized the standard Lanthanum hexaboride reference material (nano LaB_6), its measurement on the diffractometer was performed between 2θ =10°-80° with a step of 0.02°. For the LaB_6 refinement, the CIF #1000055 was inserted as the initial model and the Thompson-Cox-Hastings (TCH) pseudo-Voigt Axial divergence asymmetry function was used to obtain the instrumental parameters of the equipment which is added to the instrumental resolution file (IRF), and later used to determine the average crystallite sizes of the CeO_2 and TiO_2..

2.2.μ-Raman experimental details

Structural and vibrational features of the nano powders were analyzed by Raman spectroscopy using a confocal μ-Raman microscope inVia™ by Renishaw. The spectrometer was configurated with a 1200 grooves/mm diffraction grating and a ×50 objective with N.A. 0.75 and working distance of 0.37 mm. The excitation wavelength was set to 785 nm from a laser diode. Laser power was set to ~ 1 mW. After identifying the main Raman peaks, we use a phonon confinement model (PCM) for the estimation of nanocrystals size [18-19].

3. Results and Discussion

3.1 p-XRD analysis

p-XRD diffractograms for CeO_2 and TiO_2 NPs are shown in Figure S1(a-b). For CeO_2, it indicates a monophasic phase and could be indexed to a cubic structure. The commercial TiO_2 powder presents two characteristic crystal phases: rutile and anatase [20]. Figure S1 (b) shows the TiO_2 diffractogram which only detected the Bragg peaks of anatase phase as there is no diffraction lines that have a rutile-phase TiO_2.

3.2 Scherrer method

Scherrer obtained his equation for the ideal condition of an ideal parallel, infinitely narrow, and monochromatic X-ray beam diffracting on a monodisperse powder of cubic-shaped crystallites [21]. The broadening of the diffracted Bragg peak in the nanocrystals is due to the crystallite size and the intrinsic strain effects. This broadening often consists of one physical and instrumental broadening parts, this last one can be corrected with the following relationship [22]:

$$\beta_D = [\beta^2_{measured} - \beta^2_{instrumental}]^{1/2} \qquad (1)$$

where β_D is the corrected peak broadening. The instrumental broadening and physical broadening of the sample have been measured as FWHM. So, with the Scherrer method we can calculate the average particle size ignoring the contribution of the strain, the average crystallite size is calculated by the following equation:

$$D = \frac{K\lambda}{\beta_D cos\theta} \qquad (2)$$

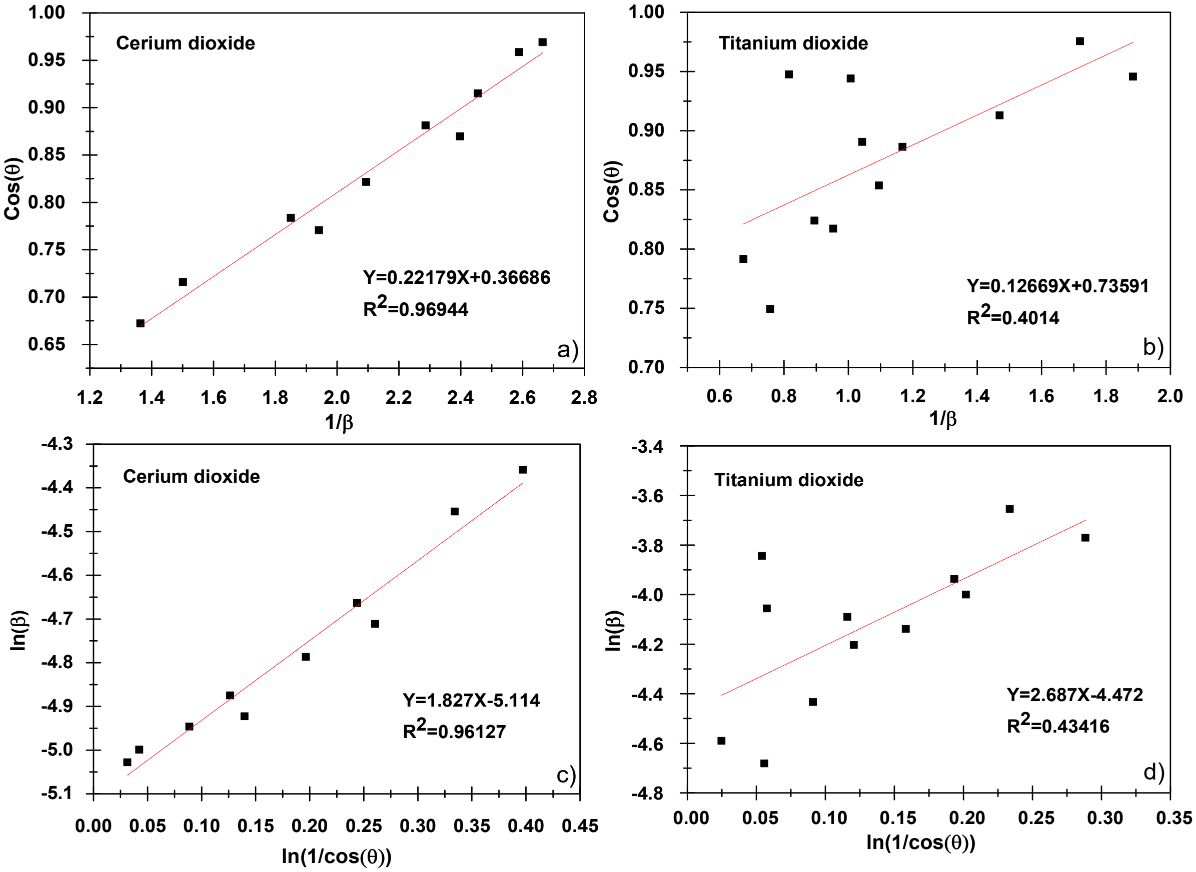

Figure 1: Scherrer plot (a,b) and Modified Scherrer plot (c,d) of CeO_2 and TiO_2 NPs.

where K is the morphological parameter or shape factor for spherical particles equal to 0.94 nm^{-1}, the wavelength (λ) of the radiograph is 1.54056 Å for $CuK_{\alpha 1}$ radiation, the Bragg diffraction angle (θ) and the FWHM is rewritten as β_D and expressed in radians. The plot $1/\beta_D$ vs $cos\theta$ shown in Figure 1a gave R^2 values higher for the CeO_2 NPs than TiO_2 NPs (Figure 1b). To have accurate results it is important to highlight that the Scherrer equation can only be used in: i) for average sizes up to 100-200 nm, ii) sample and signal/noise ratio, because the broadening of the XRD peak decreases as the crystallite size increases and it is difficult to separate the broadening from the peak [21].

3.3 Monshi method

Monshi [6] introduced some modifications to the Scherrer equation. Scherrer's equation has been seen to show an increment in the nanocrystalline size values as the d_{hkl} (diffracted planes distance) values decrease and the 2θ values increase, as $\beta cos\theta$ cannot be kept constant. The modified Scherrer equation depends on the fact that the crystallite size is obtained during each main peak and the error in crystallite size assessment is reduced, due the advantage of reducing the sum of absolute values of errors $\sum(\pm\Delta ln\beta)^2$ [23].

$$\beta_D = \frac{K\lambda}{Dcos\theta} = \frac{K\lambda}{D}\frac{1}{cos\theta} \quad (3)$$

$$ln\beta_D = ln\left(\frac{K\lambda}{D}\right) + ln\left(\frac{1}{cos\theta}\right) \quad (4)$$

Plot $ln\left(\frac{1}{cos\theta}\right)$ vs $ln\beta_D$, we can observe a straight line with a slope of around one and an intercept of $ln\left(\frac{K\lambda}{D}\right)$ from which it was calculated the average crystallite size, see Figures 1 (c) and (d). As we can see in Figure 1 (d), the value of R^2 increases with respect to the Scherrer equation. This is because if there are different *N* peaks in the range of 2θ =20°-100° it is assumed that all these peaks should represent equal values for the crystallite size. But as seen in the development of this research for each peak a different value was obtained and there is a systematic error in the results for each peak, this correction gave us a decrease in the average crystallite sizes obtaining 24.1 nm for CeO_2 and 12.7 nm for TiO_2 NPs, respectively.

3.4 W-H method

In comparison to the Scherrer formula, the W-H method considers the effect of strain-induced in the XRD peak broadening and can be used for the calculation of intrinsic strain separated from crystallite size. As already mentioned, the broadening of the physical line of the XRD peak occurs due to the size and micro-deformation of the nanocrystals. Therefore, the total broadening can be written as [22]:

$$\beta_{total} = \beta_{size} + \beta_{strain} \quad (5)$$

where, β_{size} is the broadening due to size and β_{strain} the broadening due to strain. In the next section we will analyze the crystallite size and micro-deformation using the modified W-H equation as UDM, USDM, and UDEDM.

3.4.1 UDM method

The UDM assumes that the deformation is uniform along the crystallographic direction, so this model considers the deformation, which is isotropic nature and is also known as isotropic deformation model (ISM). The intrinsic deformation affects the physical broadening of the XRD profile and the broadening β_s is related to the effective stress and Bragg angle by the equation [24]:

$$\beta_{strain} = 4\varepsilon tan\theta \quad (6)$$

where the deformation ε can be calculated from the expression $\varepsilon = \frac{\beta_{hkl}}{4tan}$. Therefore, the total broadening β_{hkl} representing the FWHM of a diffracted peak due to the contribution of the lattice strain β_{strain} and the size of the β_{size} crystallites in a particular peak that can be expressed as:

$$\beta_{hkl} = \beta_{strain} + \beta_{size} \quad (7)$$

$$\beta_{hkl} = \frac{K\lambda}{Dcos\theta} + 4\varepsilon tan\theta \quad (8)$$

Eq. (8) can be mathematically represented by:

$$\beta_{hkl}cos\theta = \frac{K\lambda}{D} + 4\varepsilon sin\theta \qquad (9)$$

From the slope of the straight line between $4sin\theta$ and $\beta_{hkl}cos\theta$ the strain can be estimated and the average crystallite size can be estimated by extrapolation of the Y-intercept Eq. (10); see Figures 2 (a) and (b) .

$$D = \frac{K\lambda}{intercept\ (y)} \qquad (10)$$

By taking the $\beta inst$ = 0.01°, we obtained the average crystallite size of the y-intercept from the linear fit. Values of 28.9 nm for the CeO_2 and 16.3 for TiO_2 NPs were obtained, respectively. In principle, this method is not realistic at all due to the consideration of isotropic nature.

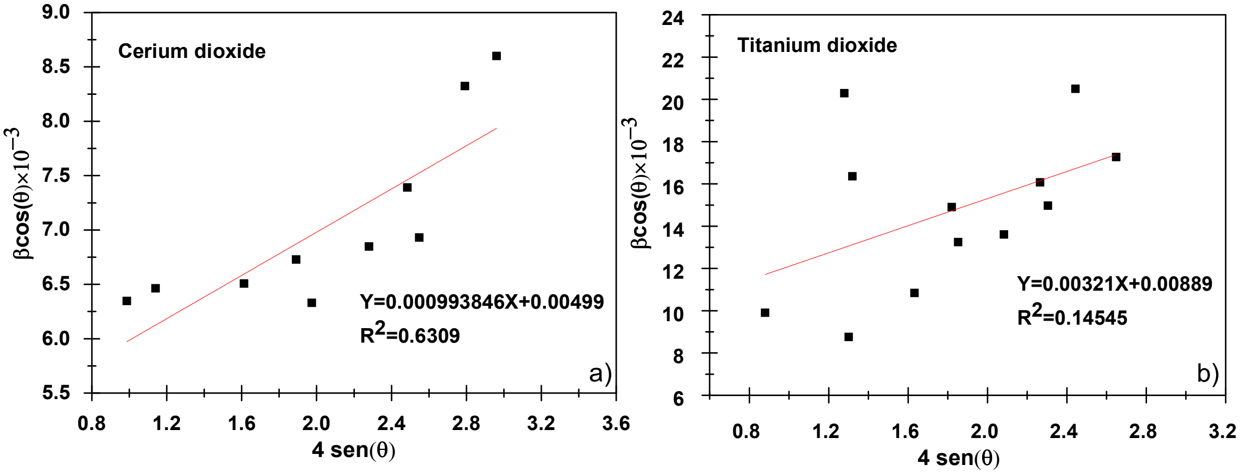

Figure 2: The W-H analysis of CeO_2 (a) and TiO_2 (b) NPs, assuming UDM model**.**

3.4.2 USDM method

This model takes into account the uniform deformation stress for a more realistic crystalline system where the anisotropic nature is considered. In addition to the uniform deformation energy density, the anisotropic nature of the Young's modulus of the crystal is more realistic [2].

Remembering Hooke's law, within the elastic limit, there is a linear proportionality relationship between strain (ε) and stress (σ), the constant of proportionality being the modulus of elasticity or simply Young's modulus and is given by $\sigma = y_{hkl}\varepsilon$, where the constant of proportionality is the modulus of elasticity or Young's modulus, denoted by y_{hkl}. Isolating the strain ε=σ/y and substituting in Eq. (9) we have:

$$\beta_{hkl}cos\theta = \frac{K\lambda}{\beta_D} + \frac{4\sigma sen\theta}{y_{hkl}} \qquad (11)$$

In Eq. (11), y_{hkl} depends on the crystallographic direction perpendicular to the set of planes (hkl) or the Miller indices. Next, the expressions for the cubic and tetragonal crystal system that are in relation to the elastic compliances constants (s_{ij}) and stiffness constants (c_{ij}) are presented.

i. Cubic crystal

For a cubic crystal, Young's modulus is calculated using the following equation:

$$y_{hkl} = \frac{9B_0G_v}{3B_0 + G_v} \tag{12}$$

where:

$$G_v = \frac{1}{5}(3C_{44} + 2C') \tag{13}$$

$$C' = \frac{1}{2}(C_{11} - C_{12}) \tag{14}$$

$$C_{11} + 2C_{12} = 3B_0 \tag{15}$$

The elasticity constants C_{44}, C_{11}, C_{12} for cubic crystals are 71, 380, 275 GPa respectively. Replacing this data in Eqs. (13), (14) and (15) for the calculation of Young's modulus in Eq. (12) giving a value of 187.5 GPa [25].

Young's modulus (y_{hkl}) is in the direction perpendicular to the crystalline lattice plane set (hkl), and for a cubic crystal it is represented by the following equation:

$$\frac{1}{y_{hkl}} = S_{11} - 2\left[(S_{11} - S_{12}) - \frac{1}{2}S_{44}\right]\left[\frac{h^2k^2 + k^2l^2 + l^2h^2}{(h^2 + k^2 + l^2)^2}\right] \tag{16}$$

$$S_{11} = \frac{C_{11} + C_{12}}{(C_{11} - C_{12}).(C_{11} + 2C_{12})} \tag{17}$$

$$S_{12} = \frac{-C_{12}}{(C_{11} - C_{12}).(C_{11} + 2C_{12})} \tag{18}$$

$$S_{44} = \frac{1}{C_{44}} \tag{19}$$

where the value of elasticity stiffness constants C_{11}, C_{12}, C_{44} for cubic CeO_2 is 455.06×10^9,188.7, $81.48 \times 10^9 \frac{\mathrm{N}}{\mathrm{m}^2}$ respectively [26]. Using these values of elasticity constants, we can calculate the elastic compliances values as 2.904×10^{-12}, -8.513$\times 10^{-13}$ and 1.227$\times 10^{-11}$, respectively. Therefore, the value of Young's modulus for each peak was calculated taking as average 262.9 GPa, this value is higher than the value calculated in Eq. (12) because the (hkl) planes are taken into account.

ii. Tetragonal crystal

Young's modulus is given by the following relation [2]:

$$\frac{1}{y_{hkl}} = \frac{S_{11}(h^4 + k^4) + (2S_{12} + S_{66})h^2k^2 + (2S_{13} + S_{44})(h^2 + k^2)l^2 + S_{33}l^4}{(h^2 + k^2 + l^2)^2} \tag{20}$$

where S_{11}, S_{12}, S_{13}, S_{33}, S_{44} are elastic strain for TiO_2 anatase, their values are $5.1 \times 10^{-12}, - 0.8 \times 10^{-12}, -3.3 \times 10^{-12}, 10.7 \times 10^{-12}, 18.5 \times 10^{-12}$, and $16.7 \times 10^{-12}\mathrm{N/m}^2$, respectively [27]. Using these elastic strains, the value of Young's modulus for each peak was calculated by taking as average 127 GPa.

Figure S2 (a-b) shows a plot between $4sen\theta/y_{hkl}$ vs $\beta_{hkl}cos\theta$, a linear fit was done where the slope represents the strain, and the average crystallite size was calculated of the intersection with the axis obtaining a value of 27.5 nm for CeO_2 and 13.4 nm for TiO_2. As mentioned, in contrast to the above method, this model uses the corresponding Young's modulus.

3.4.3 UDEDM method

It has been seen that the UDM model assumes an homogeneous crystal which is isotropic in nature. This homogeneity and isotropy is no longer justified for a real crystal. Since a crystal is anisotropic, the W-H equation must be modified by anisotropic terms [8]. This modified model is the USDM model which assumes a linear relationship between stress and strain, according to Hooke's law. But, in real crystals, the isotropic nature and linear proportionality between stress and strain cannot be considered, because there are several defects, such as dislocations and agglomerations that create imperfections in almost all crystals.

Thus, we have the UDEDM which considers the deformation of crystals, the uniform anisotropic deformation of the lattice in all crystallographic directions, and the cause of that uniform anisotropic deformation of the lattice is the deformation energy density (u). Therefore, the proportionality constants associated with the stress-strain relationship left to be independent. The strain energy (energy per unit volume) as a function of strain is given by Hooke's law as:

$$u = \frac{(\varepsilon^2 y_{hk}\ )}{2} = \frac{\sigma^2}{2y_{hk}} \qquad (21)$$

where stress and strain are related as $\sigma = \varepsilon \times y_{hkl}$, so the intrinsic strain can be written as a function of energy density.

$$\varepsilon = \sigma\sqrt{\frac{2u}{y_{hk}}} \qquad (22)$$

The W-H equation is modified in the UDEDM by:

$$\beta_{hkl} cos\theta = \frac{K\lambda}{D} + 4sen\theta\left(\frac{2u}{y_{hk}}\right)^{1/2} \qquad (23)$$

Plot of Eq (23), whit the term $4sen\theta\left(\frac{2}{y_{hkl}}\right)^{1/2}$ along X-axis and $\beta_{hkl} cos\theta$ along Y-axis corresponding to each diffraction peak where the density of energy is obtained from the slope and the average crystallite size is got from the y-intercept of the linear fitting. Figure S2 (c-d) represents the UDEDM fitted plots for CeO_2 and TiO_2 NPs, respectively. The points are from experimental data and the fitted data are shown with a straight line. The calculated parameters of this model are summarized in Table 1. With this method the estimated crystallite size was 28.5 and 15.1 nm, with R^2 values equal to 0.681 and 0.129 for CeO_2 and TiO_2, respectively. This fit is not as good comparison to previous methods. The strain values obtained for these samples were 1.287×10^{-3}, 2.42×10^{-3} and the stress values were 2.87×10^{4}, 2.18×10^{4} for CeO_2 and TiO_2, respectively.

3.5 SSP method

This method has a better result for isotropic broadening, since at higher diffracted angles , the XRD data are of lower resolution and the peaks overlap [28]. Figure 3 (a) and (b) show the linear-regression plots obtained for CeO_2 and TiO_2 NPs, respectively.

The SSP is one of the methods that considers the XRD peak profile to be a combination of the Lorentzian and the Gaussian functions. In this assumption, the strain profile is shown by the Gaussian function and the size of the crystallites by the Lorentz function.

$$\beta_{hkl} = \beta_L + \beta_G \tag{24}$$

where β_L and β_G are the broadening peak due to the Lorentz and Gauss functions, respectively. The SSP equation is presented below:

$$(d_{hkl}\beta_{hkl}cos\theta)^2 = \frac{K\lambda}{D}\left(d_{hkl}{}^2\beta_{hkl}cos\theta\right) + \frac{\varepsilon^2}{4} \tag{25}$$

In this particular method, less value is given to high angle diffraction data as an advantage it gives less weight to these, where the precision is usually lower [11]. This is because, at higher angles, XRD data are of lower quality and peaks are generally highly overlapped at higher diffracting angles [22]. It was clearly observed that the average crystallite size obtained for both CeO_2 and TiO_2 NPs are smaller compared to Scherrer's method, this difference can be given by the deformation. Therefore, when using a method that does not consider stress, it can give us inaccurate results [29]. It seems that the reason why the crystalline size decreases with this method is due to the deformation of the compounds, that is uniform and hence the peak broadening is reduced.

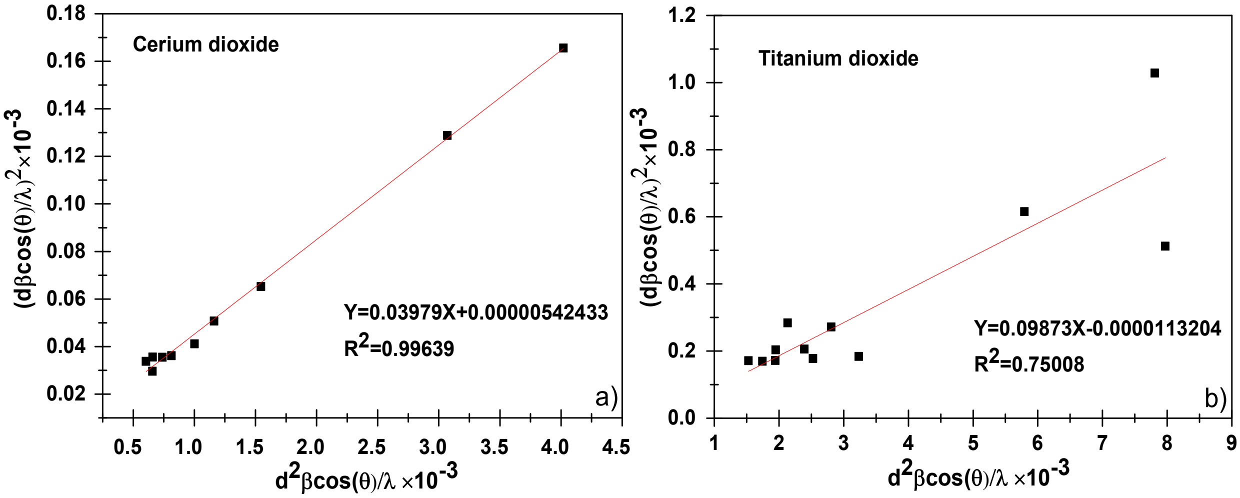

Figure 3: The SSP of CeO_2 (a) and TiO_2 NPs (b).

3.6 H-W method

In the above method, the XRD peak profile size extension has been assumed as a Lorentzian function, while strain broadening, as a Gaussian function. But actually, the XRD peak is neither Lorentzian function nor Gaussian function, as XRD peak region matches well with the Gauss function, whereas its tail falls off too fast matched and; on the other hand, the profile tails fit quite well with the Lorentz function but does not full the total area of the Bragg diffracted peak [22]. That is why H-W method is proposed, which is based on the assumption that peak broadening is a symmetric Voigt function which is a convolution of Lorentz and Gauss's function. Hence, for Voigt function, the full width at half maximum of the physical profile can be written by H-W method as:

$$\beta^2{}_{hkl} = \beta_L \beta_{hk} + \beta_G^2 \qquad (26)$$

where, β_L and β_G are the full width at half maximum of the Lorentzian and Gaussian function. This method gives more weight to Bragg peaks in the low angle range and middle angle, where overlap of diffractant peaks is low. Now, the relationship between the size of the crystallite and the lattice strain according to the H-W method is given by [22]:

$$\left(\frac{\beta^*{}_{hkl}}{d^*{}_{hkl}}\right)^2 = \frac{1}{D} \times \frac{\beta^*{}_{hkl}}{d^*{}_{hkl}{}^2} + \left(\frac{\varepsilon}{2}\right)^2 \qquad (27)$$

where $\beta^*{}_{hkl} = \beta_{hkl} \times \frac{cos\theta}{\lambda}$ and $d^*{}_{hkl} = 2 \times d_{hkl} \times \frac{sin\theta}{\lambda}$, plot $\frac{\beta^*{}_{hkl}}{d^*{}_{hkl}{}^2}$ vs $\left(\frac{\beta^*{}_{hkl}}{d^*{}_{hkl}}\right)^2$ is shown in the Figure 4 [28]. The slope of the plotted straight line provides the average crystallite size; these have been calculated from Figures 4 (a) and (b) obtaining values of 10.4 and 5.1 nm for CeO_2 and TiO_2 NPs, respectively. Also, the intercept gives the intrinsic strain of the nanocrystals. We can observe that the H-W method is more accurate. In Figures 4 (a) and (b), we can regard a greater approach of the fit line to the experimental data for both NPs as a result of the integral broadening to a Voigt function.

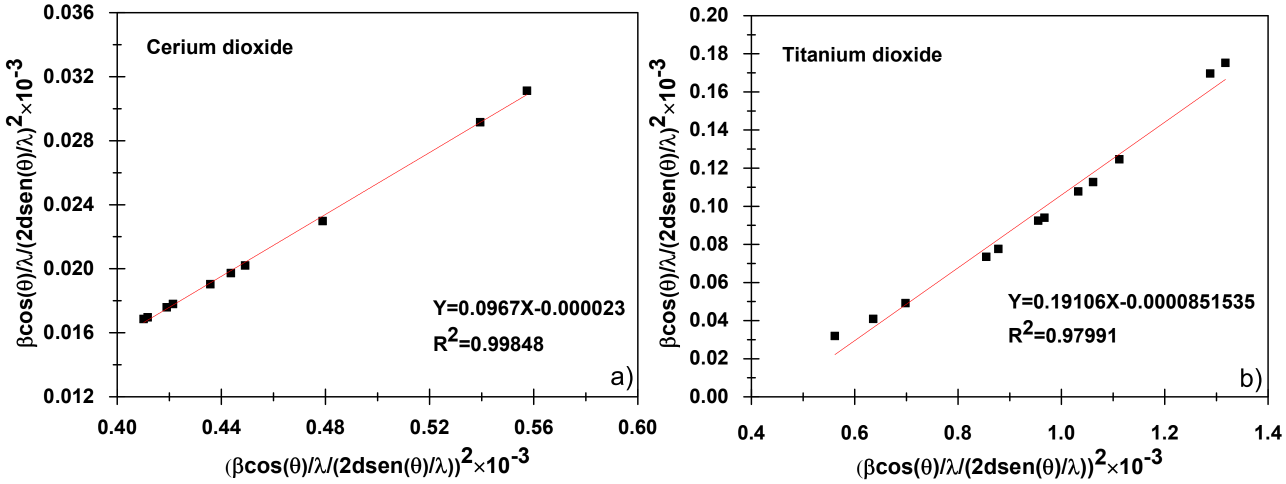

Figure 4: H-W plot of CeO_2 (a) and TiO_2 (b).

By comparing the results of the crystallite size and lattice strain, shown in the Table 1, we can see that the H-W method shows a decrease in crystallite size as well as lattice strain, a common feature between the W-H and H-W method is that the dispersion of data points increases with increased lattice strain, which would indicate that lattice strain is anisotropic [30], but in our case you see a decrease in the dispersion of the points and also a decrease in deformation so you could say that lattice strain is isotropic in nature.

Table 1. Microstructural parameters of the CeO_2 and TiO_2 NPs obtained by several crystalline size analysis methods.

		Samples	**CeO_2**	**TiO_2**
Scherrer method		D (nm)	20.8	10.5
		R^2	0.969	0.401
Modified Scherrer method		D (nm)	24.1	12.7
		R^2	0.961	0.434
Williamson-Hall method	UDM	D(nm)	28.9	16.3
		$\varepsilon \times 10^{-3}$	0.994	3.21
		R^2	0.631	0.146
	USDM	D (nm)	27.5	13.4
		$\varepsilon \times 10^{-3}$	9.852	28.4
		σ (MPa) × 10^2	2.19	2.56
		R^2	0.674	0.076
	UDEDM	D (nm)	28.5	15.1
		$\varepsilon \times 10^{-3}$	1.287	2.422
		σ (MPa) × 10^4	2.87	2.18
		U (TJm^{-3})	0.018	0.026
		R^2	0.681	0.129
Size-Strain Plot method		D (nm)	18.9	7.6
		$\varepsilon \times 10^{-3}$	4.653	6.751
		R^2	0.996	0.75
Halder Wagner method		D (nm)	10.4	5.1
		R^2	0.999	0.979
		$\varepsilon \times 10^{-3}$	9.584	18.62
Rietveld Refinement		D (nm)	12 (4)	14.1 (4)
		ε	20.41	137.66
µ-Raman		D (nm)	14.5	11.5
TEM		D (nm)	10-20	5.2-16.3

The R^2 values are important to differentiate among all of the studied linear methods (see Table 1). We obtained only positive values of R^2 for all of the crystallographic phases, one method is more accurate if the R^2 is near 1 or in other words, data points of x-y are more touching the fitting line [31]. The H-W method is more accurate, suggesting that this model better fits the XRD diffractograms presented in this study.

3.7. Rietveld Refinement

Figures 5 (a) and (b) shows the refined diffractogram of CeO_2 and TiO_2 NPs using the TCH profile functions, and the refined parameters are displayed in Table 2. For CeO_2 NPs, the RM confirms the cubic structure of the CeO_2 NPs where the characteristic peaks are very close to the fluorite-structured CeO_2 crystal and no peak of any other phase was detected, indicating the high purity of the sample. For TiO_2, the corresponding tetragonal structure of the TiO_2 NPs shows the presence of anatase phase only. The weighted profile residual (R_{wp}) and the profile residual factor (Rp) were taken into account to follow the progress and as indicator of the refinement improvement. The goodness of refinement, χ^2 (chi-squared), indicates the statistical error. In both samples, small values of 1.94 and 2.25 were obtained using the TCH profile for TiO2 and CeO_2 NPs, respectively.. For the estimation of the mean crystallite size the TCH profile was used, for which an IRF file is yielded by fitting the XRD diffractogram of the LaB_6 nano-standard, which subtracts the instrumental broadening. The mean apparent size was 12 and 14.1 nm, for the CeO_2 and TiO_2 nanocrystallites, respectively, and of 40.5 nm for the LaB_6 standard (see Figure S3 (a-d) and Table S1).

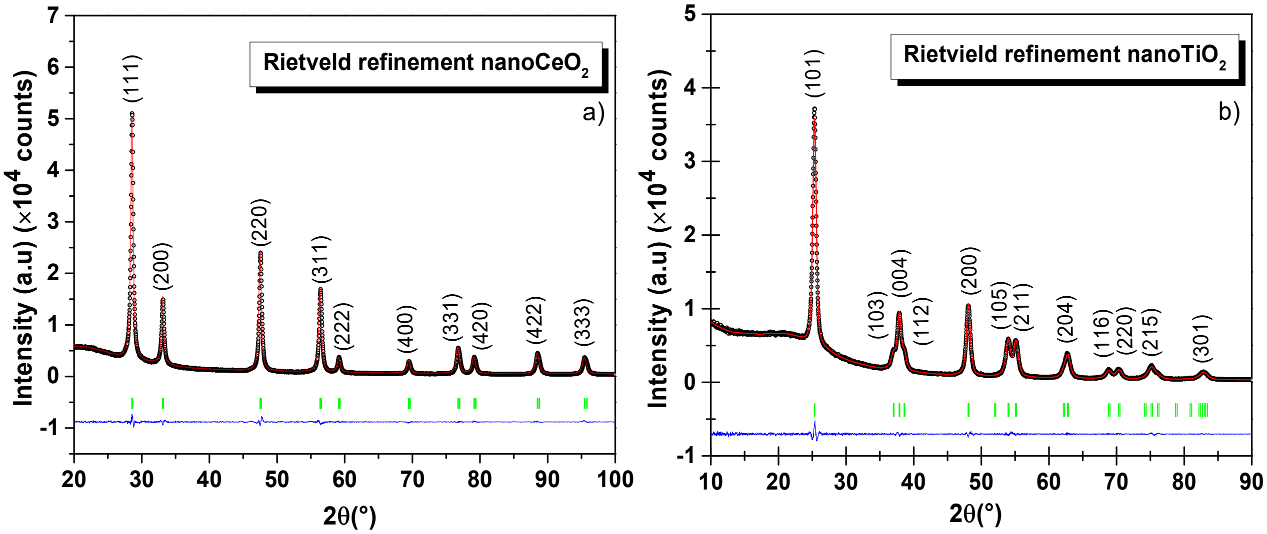

Figure 5. Rietveld refinement of XRD diffractograms using the TCH function for CeO_2 (a) and TiO_2 NPs (b). The observed experimental diffractograms are given by the red lines (I_{obs}), the black lines (I_{cal}) are calculated diffractograms, and the residual lines are shown in blue color. The refinement parameters are reported in Table 2.

3.8 Electron density modeling

Electronic density measures the probability of finding an electron in a certain region of the atom. The higher the concentration of electrons at a given point, the higher the electronic density. Therefore, depending of the material will exhibit certain characteristics. It can be seen on a scale composed of rainbow colors, red to indicate the region of highest electronic density and blue for that region where there are fewer electrons. Figures 6a and 6b show that there is no formation of ionic bonds using as an indicator the red color that are the covalent bonds. The Vesta program was used with a resolution of 0.6 Å for both samples.

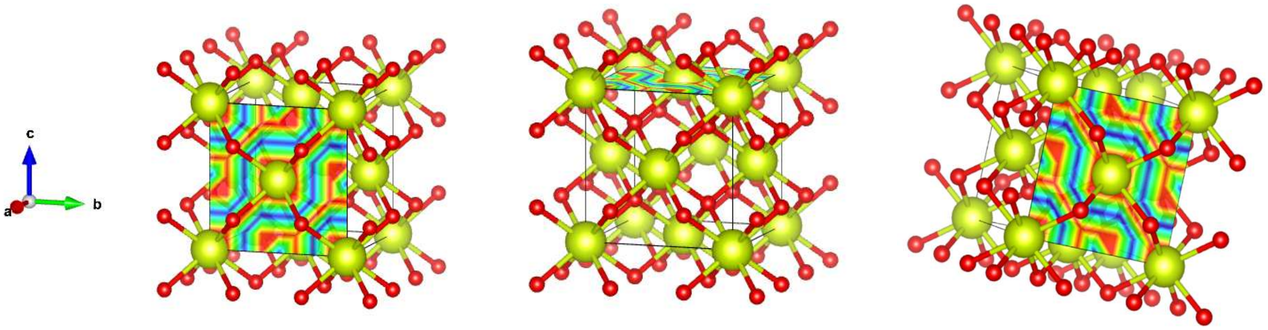

(a) (b) (c)

Figure 6a. Electron density model with 0.6 Å resolution of nanoCeO_2 for the (hkl) lattice planes (1 0 0) (a), (0 0 1) (b) and (0 1 0) (c).

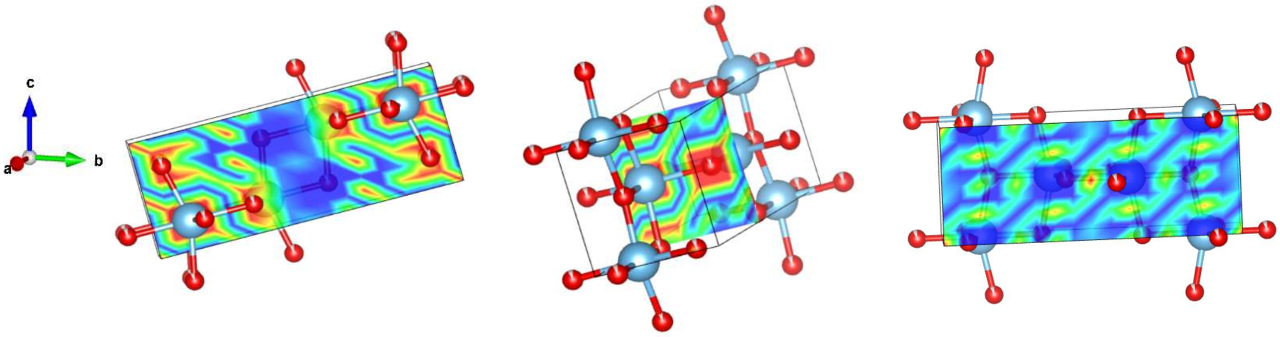

(d) (e) (f)

Figure 6b. Electron density model with 0.6 Å resolution of nanoTiO_2 for the (hkl) lattice planes (1 0 0) (a), (0 0 1) (b) and (0 1 0) (c).

3.9. µ-Raman analysis

For spherical particles with a diameter D and no vibration mode degeneration, the Raman intensity can be written as shown in Eq. (28)

$$I(\omega) \propto \int_{BZ} d^3q \, \frac{|C(q,D)|^2}{(\omega-\omega(q))^2+\left(\frac{\Gamma}{2}\right)^2} \tag{28}$$

Here, q is the phonon wave vector ranging in the BZ from $-\pi/a$ to π/a, with a the lattice parameter. The volume differential d^3q under the spherical symmetry approximation is written as $d^3q = 4\pi q^2 dq$. Γ is the intrinsic mode line width of the Lorentzian response centered at $\omega(q)$, with $\omega(q)$ the phonon dispersion relation, $C(q, D)$ are the Fourier coefficients of a weighting function describing the confinement, i.e. enforcing the decay of the phonon wave function to a minimal value close to the nanocrystal boundary.

$$|C(q,D)|^2 = \left(-\frac{q^2D^2}{8\beta}\right) \tag{29}$$

According to previous reports, for particle diameters greater than $D \geq 10$ nm [17, 18, 32], a Gaussian confinement weighting function is a good approximation, and thus the Fourier coefficients are written as depicted in Eq. (29). The confinement factor β can vary from 1 to $2\pi^2$ for the Ritchter confinement model [33] and Campbell model, respectively [34]. Here, for the sake of simplicity we fix $\beta = 1$. Previous reports suggest that the dispersion relation for anatase TiO_2 NPs near the E_g band can be modeled as $\omega(q) = \omega_0 + \Delta(1 - cos\,(qa)\,)$ with $\Delta = 20\ cm^{-1}$. For the case of CeO_2 NPs, we simply approximate the dispersion relation with a polynomial function of order 3, $\omega(q) = \omega_0 + A_1 q + A_2\, q^2 + A_3\, q^3$. Distinct reports put ω_0 for the F_{2g} mode between 464 and 466 cm^{-1}. Here the best fitted value is obtained for ω_0=464.4 cm^{-1} in agreement with Spainer et al [32]. However, our analysis did not include strain effects.

In order to fit Eq. (28) we normalize the Raman intensity to the peak area. We do this with the experimental data and with Eq. (28). The fitting procedure is based on the minimization of the unbiased squared error with free parameters ω_0, L and Γ.

Figure 7 a and b, depict the Raman spectra of the TiO_2 and CeO_2 NPs, respectively. For the TiO_2 NPs the E_g and B_{1g} bands are identified. The A_{1g} band cannot be resolved. The analysis is performed with the E_g band centered at 144 cm^{-1}. The characteristic F_{2g} band at 464 cm^{-1} of the CeO_2 particles is observed and used for the analysis. Both peaks were fitted using Eq. (29) after normalization. The estimated NPs size are 11.5 nm and 14.5 nm for TiO_2 and CeO_2, respectively with a fitting error close to 0.01 nm. Additional error source could be attributed to a particle size distribution not considered in this analysis.

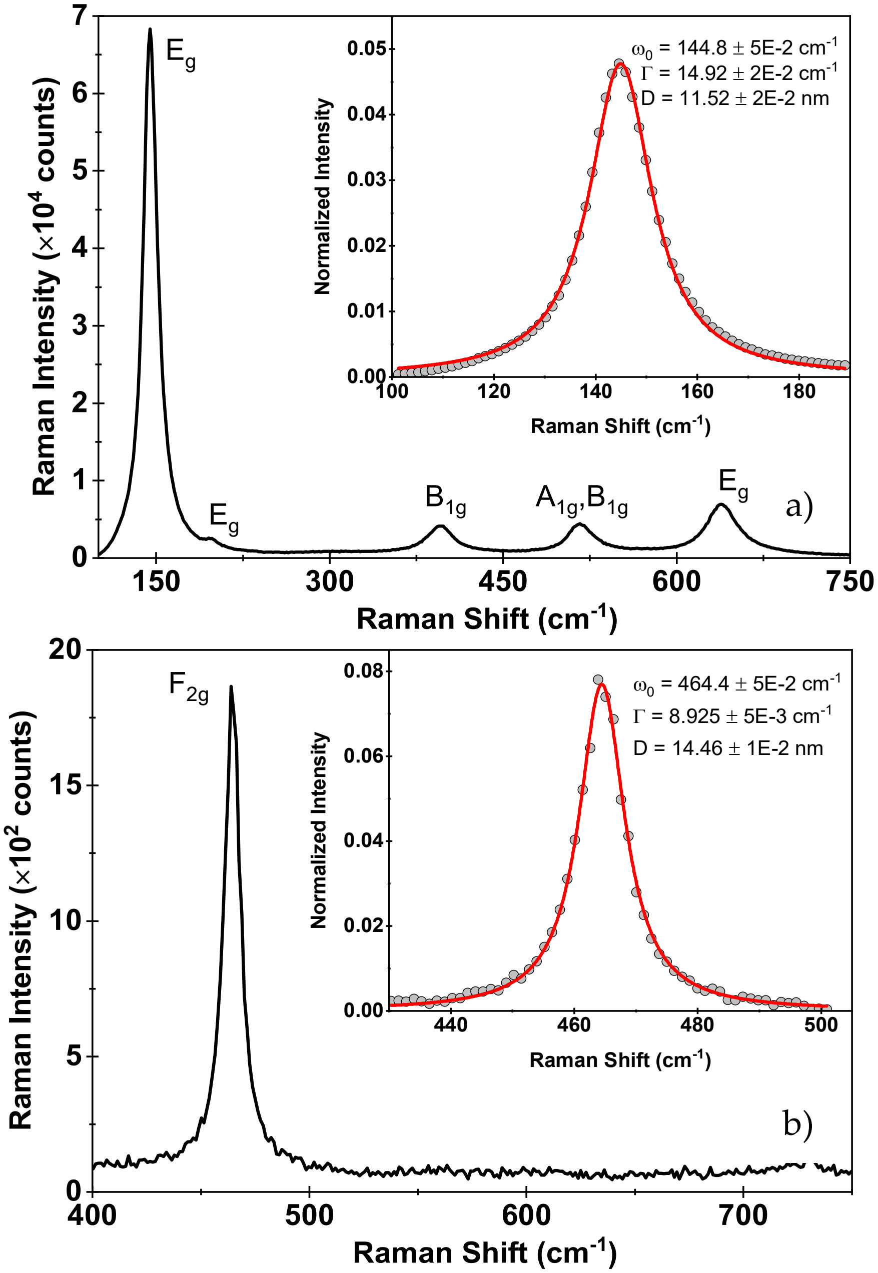

Figure 7. Raman spectrum of TiO_2 (a) and CeO_2 (b) nanopowders, respectively. Inset graphs denotes the fit after Eq. 29. Best fitted parameters are shown.

3.10. TEM analysis and comparison

Commercial nanoceria NPs have average TEM particle sizes in the range of 15-25 nm [35]. The nanoceria are agglomerated and present a particle size distribution (PSD). While the crystallite estimation methods including Rietveld refinement, gave values between 10 and 20 nm, which is reasonable agreement with TEM determination and hence suggesting that the Scherer, W-H, SSP, and H-W methods are accurate suggesting the presence of PSD. On the other hand, donut-like TiO_2 NPs shown in Figures 8(a) and (b) shows a particle size of ca. 20 nm with mean pore sizes of 5-7 nm. By comparing with the size estimation methods, the crystallite sizes are in the interval of 5.2 to 16.3 nm. Then the anatase TiO_2 NPs is composed of these individual crystallites. It can be concluded that in the case of PSD, the NPs are formed by nanocrystallites with anisotropic size behavior, then a crystallite size distribution is expected By comparing all the methods, it can be said that the crystallite sizes obtained by the W-H method are more accurate, but an overestimation of 35% with respect to Scherrer method is obtained, as shown in TiO_2 NPs, where W-H crystallite sizes are on average 3-5 nm times higher than the sizes of the Scherrer equation [36]. Moreover, the H-W method underestimate the crystallite size obtained from Rietveld method in ca. 5 nm. This suggest that the strain contribution must be considered in the sample with exotic morphologies as compared with nanoceria.

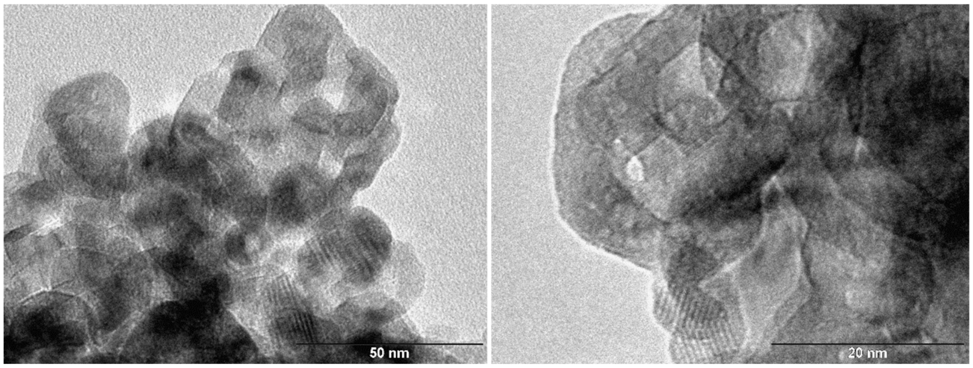

(a) (b)

Figure 8. TEM image of nano-TiO_2 with bar length of 50 nm (a) and bar length of 20 nm (b).

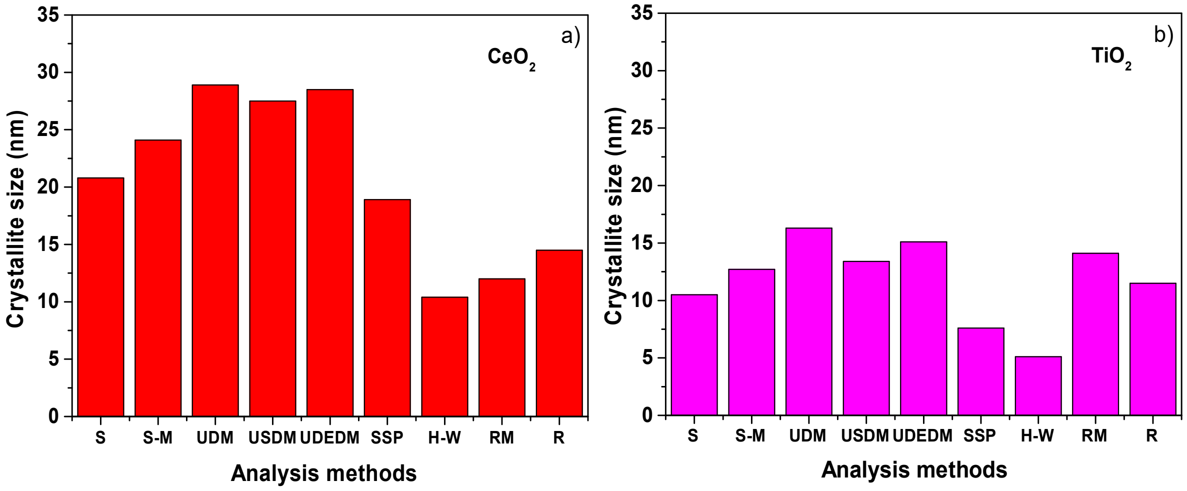

Figure 9. Comparison of the average crystallite size obtained by different estimation methods S (Scherrer method), RM (Rietveld Refinement), R (μ-Raman) for CeO_2 (**a**) and TiO_2 NPs (**b**).

Figures 9 (a) and (b) shows the the crystallite size values as a function of the different methods based on the analysis of the line profiles using the p-XRD, showing a variation except in the three W-H models, as reflected in the data fit shown in the previous Figures. In the case of the H-W method, it shows a decrease in the crystallite size, which confirms the nanostructured character presented in the sample. On the other hand, the RM is consistent with the size strain method. This provides reliability in the method and allows its use to obtain average crystallite sizes, being one of the most important part in the characterization of nanomaterials.

Table 2. Rietveld refinement parameters of CeO_2 and TiO_2 samples using the Fullprof program: cell parameters, cell volume and agreement factors. R_p (%) and R_{wp} (%) are the profile residual and the weighted profile residual factors, respectively, used to verify the Rietveld refinement quality. The goodness of fit, chi-square (χ^2).

Refinement Parameters	**nanoCeO_2**		**nanoTiO_2**	
	TCH	**Pseudo Voigt**	**TCH**	**Pseudo Voigt**
a (Å)	5.408	5.409	3.784	3.784
b (Å)	5.408	5.409	3.784	3.784
c (Å)	5.408	5.409	9.502	9.504
α (Å)	90	90	90	90
β (Å)	90	90	90	90
γ (Å)	90	90	90	90
V (Å^3)	158.14	158.28	136.03	136.11
FWHM parameters				
U	0.085	0.098	2.708	6.218
V	-0.589	-0.030	-1.784	-3.384
W	0.014	0.105	0.775	1.129
Global average size (nm)	12.0 (4)		14.1 (4)	
R_p (%)	5.40	4.83	7.11	6.86
R_{wp} (%)	5.42	5.01	6.33	6.19
χ^2	2.25	1.93	1.94	1.99

4. Conclusion

In this work, an exhaustive analysis of XRD data for CeO_2 and TiO_2 NPs are presented using crystallite size estimation methods, among them: the Scherrer method, the Monshi method, the W-H model, the UDM, UDEDM, SSP, and H-W method, where all of them suggested an important isotropic broadening contribution, assuming Lorentzian and Gaussian profile contributions to estimate the crystallite size and microdeformation physical parameters. However, the method of Scherrer and W-H have less precision for the determination of the crystallite size for these metallic nanooxides. Furthermore, the crystallite size was calculated using the RM. Fort that, the IRF function was considered and obtained from the refinement of the standard (nano LaB_6). By employing the RM, it was possible to carry out the refinement of CeO_2 and TiO_2 nanopowders corroborating the phases of cubic nanoCeO_2 and TiO_2 anatase using the TCH profile and hence allowing calculation of microstructural parameters. After comparing all the presented models, it was found that the average crystallite sizes determined by the SSP and H-W methods are close to the results obtained in RM, in case of the CeO_2, but for the TiO_2 the Monshi method was the closest model. Then, we can say that the average crystallite size of CeO_2 and TiO_2 NPs are in a range of 10-15 nm as also corroborated by TEM analysis. Thus, suggesting that each NP is made up of two or at least three crystallites. Crystallite size determined by Raman analysis are in agreement with this particle crystallite distribution. Therefore, we have presented in detail XRD characterization that strongly correlates with Raman and TEM analysis. This perspective can be used in future works in order to analyze and estimate accurately the cystallite size distribution presented in NPs as prepared by different physical and chemical methods as well.

Supplementary Materials: Figure S1. Pure p-XRD pattern of CeO_2 (a) and TiO_2 NPs (b). Figure S2. The modified W-H analysis of CeO_2 (a) and TiO_2 NPs (b), assuming USDM. The modified W-H analysis of CeO_2 (c) and TiO_2 NPs (d), assuming UDEDM. Figure S3**.** Rietveld refinement using the TCH function for LaB_6 (a). The observed experimental diffractograms are given by the red lines (I_{obs}), the black lines (I_{cal}) are calculated diffractograms, and the residual lines are shown in blue color. Electron density model with 0.4 Å resolution of LaB_6 for the (hkl) lattice planes (1 0 0) (b), (0 0 1) (c), and (0 1 0) (d). Supplementary Matlab code R2017b.

Author Contributions: Conceptualization, Y.C.H., A.F. M.A., J.P.V. Y.B.R., J.A.G. and J.A.R.G.; methodology, Y.C.H., A.F. M.A., J.P.V. Y.B.R., J.A.G. and J.A.R.G.; software, Y.C.H., A.F. M.A., J.P.V. Y.B.R., J.A.G. and J.A.R.G.; formal analysis, Y.C.H., A.F. M.A., J.P.V. Y.B.R., J.A.G. and J.A.R.G.; investigation, Y.C.H., A.F. M.A., J.P.V. Y.B.R., J.A.G. and J.A.R.G.; resources, Y.C.H., A.F. M.A., J.P.V. Y.B.R., J.A.G. and J.A.R.G.; data curation, Y.C.H., A.F. M.A., J.P.V. Y.B.R., and J.A.G.; writing—original draft preparation, Y.C.H., A.F. M.A., J.P.V. Y.B.R., J.A.G. and J.A.R.G.; writing—review and editing, Y.C.H., A.F. M.A., J.P.V. Y.B.R., J.A.G. and J.A.R.G.; visualization, Y.C.H., A.F. M.A., J.P.V. Y.B.R., J.A.G. and J.A.R.G.; supervision, J.A.R.G.; project administration, J. A.R.G; funding acquisition, J.A.R.G. All authors have read and agreed to the published version of the manuscript.

Funding: This research was funded by Fondo Nacional de Desarrollo Científico, Tecnológico y de Innovación Tecnológica (FONDECYT-CONCYTEC). Project Number 177-2020-FONDECYT.

Data Availability Statement: The simulated data of the present research can be provided upon reasonable request at the email juan.ramos5@unmsm.edu.pe.

Acknowledgments: The authors thank the Fondo Nacional de Desarrollo Científico, Tecnológico y de Innovación Tecnológica (FONDECYT-CONCYTEC), project number: 177-2020-FONDECYT, and acknowledge the support of the Center of Materials Characterization of the Pontificia Universidad Católica del Peru (CAM-PUCP).

Conflicts of Interest: The authors declare no conflict of interest.

References

1. Charles, P.; Frank J. Introducción a la Nanotecnología, 1st ed.; Reverté, Barcelona, España, 2007.
2. Rajender, G; Giri, P.K. Strain induced phase formation, microstructural evolution and bandgap narrowing in strained TiO_2 nanocrystals grown by ball milling. *J Alloys Compd.* **2016**, 676, 591–600.
3. Henao, C.P.B.; Montes, V.H.; Sierra, R.B. Nanopartículas para materiales antibacterianos y aplicaciones del dióxido de titanio. *Rev Cuba Investig Biomed.* **2016**, 35, 387–402.
4. Raez, J.M.; Arencibia, A.; Segura, Y.; Arsuaga, J.M.; López-Muñoz, M.J. Combination of inmobilized TiO_2 and zero valent iron for efficient arsenic removal in aqueous solutions, Sep. Purif. Technol. 2021, 258, 118016.
5. Goyeneche, L.M. Determinación del tamaño de partícula mediante difracción de rayos X. Fin de grado. Universidad de Cantabria, España, septiembre-2018.
6. Kunka, C.; Boyce, B.L.; Foiles, S.; Dingreville, R. Revealing inconsistencies in X-ray width methods for nanomaterials. *Nanoscale* **2019**, 11, 1-24.
7. Monshi, A.; Foroughi, M.R.; Monshi, M.R. Modified Scherrer Equation to Estimate More Accurately Nano-Crystallite Size Using XRD. *World J Nano Sci Eng.* **2012**, 02, 154–160.
8. Williamson, G.K.; Hall W.H. X-ray line broadening from filed aluminium and wolfram. *Acta Metall.* **1953**, 1, 22–31.
9. Mote, V.D.; Purushotham, Y.; Dole B.N. Williamson-Hall analysis in estimation of lattice strain in nanometer-sized ZnO particles. *J Theor Appl Phys.* **2012**, 6, 2–9.
10. Kumar, B.R.; Hymavathi, B. X-ray peak profile analysis of solid-state sintered alumina doped zinc oxide ceramics by Williamson–Hall and size-strain plot methods. *J Asian Ceram Soc.* **2017**, 5, 94–103.

11. Motevalizadeh, L.; Heidary, Z.; Abrishami, M.E. Facile template-free hydrothermal synthesis and microstrain measurement of ZnO nanorods. *Bull Mater Sci.* **2014**, 37, 397–405.
12. Tagliente, M.A.; Massaro, M. Strain-driven (0 0 2) preferred orientation of ZnO nanoparticles in ion-implanted silica. *Nucl Instruments Methods* **2008**, 266, 1055–1061.
13. Young, R.A. The Rietveld Method. International Union of Crystallography Oxford University, New York, 1993.
14. Blanco, R.C.; Casagrande, S.P. Método de Rietveld para el estudio de estructuras cristalinas. Univ Nac Ing. 2004, 2, 1–5.
15. Raquejo, D.J. Desarrollo de un protocolo para la aplicación del método de Rietveld y del estándar interno en la caracterización de materiales cerámicos con contenido de amorfos. Fin de grado. Universidad EAFIT, Medellín, 2015.
16. Pecharsky, V.J.; Zavalij, P. Y. Fundamentals of Powder Diffraction and Structural Characterization of Materials, Springer Science+Business Media, LLC 2009, 2nd Ed. ISBN: 978-0-387-09578-3. Pags. 269-292.
17. Ramos-Guivar JA, Taipe K, Schettino MA, Silva E, Torres MAM, Passamani EC, et al. Improved removal capacity and equilibrium time of maghemite nanoparticles growth in zeolite type 5A for Pb(II) adsorption. *Nanomaterials* **2020**;10(9):1–19.
18. Paillard, V.; Puech, P.; Laguna, M.A.; Carles, R.; Kohn, B.; Huisken, F. Improved one-phonon confinement model for an accurate size determination of silicon nanocrystals. *J Appl Phys.* **1999**, 86, 1921–1924.
19. Grujić-Brojčin, M.; Šćepanović, M.J.; Dohcević-Mitrovic, Z.D.; Popović, Z.V. Use of phonon confinement model in simulation of Raman spectra of nanostructured materials. *Acta Phys Pol A.* **2009**, 116, 51–54.
20. Guivar, J.A.R.; Bustamante, D. A.; Gonzalez, J.C.; Sanches, E.A.; Morales, M.A.; Raez, J.M.; et al. Adsorption of arsenite and arsenate on binary and ternary magnetic nanocomposites with high iron oxide content. *Appl Surf Sci.* **2018**; 454, 87–100.
21. Holzwarth, U.; Gibson, N. The Scherrer equation versus the "Debye-Scherrer equation" **2011**, 6.
22. Nath, D.; Singh, F.; Das, R. X-ray diffraction analysis by Williamson-Hall, Halder-Wagner and size-strain plot methods of CdSe nanoparticles- a comparative study. *Mater Chem Phys.* **2020**, 239, 1-9.
23. Khandan, A.; Ozada, N.; Karamian, E. Novel Microstructure Mechanical Activated Nano Composites for Tissue Engineering Applications. *J Bioengineering Biomed Sci.* **2015**, 5, 1–4.
24. Hall, W.H. X-ray line broadening in metals. *Proc Phys Soc A.* **1949**, 62, 741–743.
25. Jamal, M.; Asadabadi, S.J; Ahmad, I.; Aliabad, H.A.R. Elastic constants of cubic crystals. *Comput Mater Sci.* **2014**, 95, 592–599.
26. Goldsby, J.C. Basic Elastic Properties Predictions of Cubic Cerium Oxide Using First-Principles Methods. *J Ceram.* **2012**, 2013, 1–4.
27. Borgese, L.; Bontempi, E.; Gelfi, M.; Depero, L.E.; Goudeau, P.; Geandier, G. et al. Microstructure and elastic properties of atomic layer deposited TiO_2 anatase thin films. *Acta Mater.* **2011**, 59, 2891–2900.
28. Rabiei, M.; Palevicius, A.; Monshi, A.; Nasiri, S.; Vilkauskas, A.; Janusas, G. Comparing methods for calculating nano crystal size of natural hydroxyapatite using X-ray diffraction. *Nanomaterials* **2020**, 10, 1–21.
29. Zak, A.K.; Majid, W.H.A.; Abrishami, M.E.; Yousefi, R.; Parvizi, R. Synthesis, magnetic properties and X-ray analysis of Zn0.97 X0.03O nanoparticles (X = Mn, Ni, and Co) using Scherrer and size-strain plot methods. *Solid State Sci.* **2012**, 14, 488–494.
30. Al-Tabbakh, A.A.; Karatepe, N.; Al-Zubaidi, A.B.; Benchaabane, A.; Mahmood, N.B. Crystallite size and lattice strain of lithiated spinel material for rechargeable battery by X-ray diffraction peak-broadening analysis. *Int J Energy Res.* **2019**, 43, 1-9.
31. A. Gholizadeh X-Ray Peak Broadening Analysis in $LaMnO_{3+\delta}$ Nano-Particles with RhombohedralCrystal Structure. *J Adv Mater Process.* **2015**, 3, 71–83.
32. Spanier, J.E.; Robinson, R.D.; Zhang, F.; Chan, S.W.; Herman, I.P.; Size-dependent properties of CeO_{2-y} nanoparticles as studied by Raman scattering. *Phys Rev. B* **2001**, 64, 1-8.
33. Richter, H.; Wang, Z.P.; Ley, L. The one phonon Raman spectrum in microcrystalline silicon. *Solid State Commun.* **1981**, 39, 625-629.
34. Campbell, I.H.; Fauchet; P.M. the Effects of Microcrystal Size and Shape on the One Phonon Raman Spectra of crystalline Semiconductors. *Solid State Commun.* **1986**, 58, 739–741.
35. Giri, S.; Karakoti, A.; Graham, R. P.; Maguire, J.L.; Reilly, C.M.; Seal, S.; Rattan, R.; Shridhar, V.; Nanoceria: A Rare-Earth Nanoparticle as a Novel Anti- Angiogenic Therapeutic Agent in Ovarian Cancer, *PloS one* **2013**, 8, 54578.
36. Kibasomba, P.M.; Dhlamini, S., Maaza, M.; Liu, C.P.; Rashad, M.M.; Rayan, D.A. et al. Strain and grain size of TiO_2 nanoparticles from TEM, Raman spectroscopy and XRD: The revisiting of the Williamson-Hall plot method. *Results Phys.* **2018**; 9, 628–635.